



HAL
open science

An Improved Characteristic Based Volume Penalization Method for the Euler Equations Towards Icing Applications

Pierre Lavoie, Emmanuel Radenac, Ghislain Blanchard, Éric Laurendeau,
Philippe Villedieu

► **To cite this version:**

Pierre Lavoie, Emmanuel Radenac, Ghislain Blanchard, Éric Laurendeau, Philippe Villedieu. An Improved Characteristic Based Volume Penalization Method for the Euler Equations Towards Icing Applications. 2020. hal-02872954v1

HAL Id: hal-02872954

<https://hal.science/hal-02872954v1>

Preprint submitted on 18 Jun 2020 (v1), last revised 7 Apr 2021 (v2)

HAL is a multi-disciplinary open access archive for the deposit and dissemination of scientific research documents, whether they are published or not. The documents may come from teaching and research institutions in France or abroad, or from public or private research centers.

L'archive ouverte pluridisciplinaire **HAL**, est destinée au dépôt et à la diffusion de documents scientifiques de niveau recherche, publiés ou non, émanant des établissements d'enseignement et de recherche français ou étrangers, des laboratoires publics ou privés.

An Improved Characteristic Based Volume Penalization Method for the Euler Equations Towards Icing Applications

Pierre Lavoie^{a,b,*}, Emmanuel Radenac^b, Ghislain Blanchard^b, Éric Laurendeau^a, Philippe Villedieu^b

^a*Department of Mechanical Engineering, Polytechnique Montréal, C.P. 6079, succ. Centre-ville, Montréal (Qc), H3C 3A7, Canada*

^b*ONERA - The French Aerospace Lab, F-310pp Toulouse, France*

Abstract

The numerical prediction of in-flight ice accretion generally involves geometry updates and re-meshing as the ice builds up. However, the generation of body-fitted meshes around complex ice shapes is not trivial and needs to be repeated several times to obtain the final ice shape. The use of an immersed boundary method can simplify the mesh generation and help in the automation of ice accretion simulations. In this paper, the development of an immersed boundary method for Euler flows is detailed. A new penalization method is proposed to impose the conservation of entropy and total enthalpy in the normal direction to the wall instead of the classical adiabatic condition. The two approaches are compared and numerically tested on several cases: weakly compressible flow around a circular cylinder, subsonic flow around a NACA0012 airfoil and flow around a challenging high curvature ice horn. The new method is found to be more accurate on coarser meshes and better at retrieving attached flows for curved geometries. The paper concludes that the proposed method is suitable for icing simulations while being still appropriate for general aerospace applications.

Keywords: CFD, Euler Equations, Volume Penalization, Compressible Flow, Inviscid Flow, Immersed Boundary Method, Icing, Ice Accretion

1. Introduction

Numerical tools for the prediction of in-flight ice accretion have been developed and used for many years. Ice accretion is an unsteady multi-physics process where super-cooled water droplets impinge on a cold surface (e.g. aircraft wings, tail) and might freeze upon impact or run back and freeze farther downstream. This process of impingement and freezing generates ice buildups ranging from simple streamlined ice shapes to more complex geometries like ice horns, scallops and lobster tails [1]. Typical tools for the prediction of ice accretion segregate the simulation of the physics in different modules that are called sequentially in a quasi-steady approach:

1. mesh generation;
2. computation of the aerodynamics;
3. computation of the droplet trajectories and impingement rates;
4. evaluation of the convective heat transfer at the wall;
5. computation of the ice accretion (mass and heat balance);
6. geometry update (the ice shape is generated).

The ice accretion can be divided in several time steps, referred to as a multi-step process. In this case, modules 1 to 6 are embedded in a time loop where for each time step, a

mesh is regenerated (module 1), the physics is re-evaluated (modules 2 to 5) and the ice shape is updated (module 6). The process is repeated until the final ice accretion time is achieved. A mesh is generated for each time step and this can become cumbersome when a large number of steps are required. Nowadays, much interest is directed towards the simulation of complex 3D ice shapes such as scallops and lobster tails. These types of geometries are difficult to predict using numerical tools and difficult to mesh. To reduce the cost related to mesh generation and ease its automation, it is envisioned to replace the classical body-fitted meshes by the use of an immersed boundary method.

When using body-fitted (BF) meshes, the effort is spent on generating a good quality mesh that matches the geometry. On the other hand, when using an Immersed Boundary Method (IBM), the mesh generation can be much simpler (e.g. Cartesian grid) as the geometry is allowed to arbitrarily cut through the mesh. In this case the effort is spent on the correct imposition of the boundary condition. In the context of ice accretion, the use of an Immersed Boundary Method could reduce the effort invested in re-meshing (especially in 3D), and could ease the automation of 3D ice accretion tools. The first step towards the application of an Immersed Boundary Method to an ice accretion suite is its application to the aerodynamics solver which is the focus of this paper.

Although there is a higher benefit in using Immersed Boundary Methods for 3D ice accretion, the developments are performed in ONERA's 2D icing suite IGLOO2D [2]

*Corresponding author

Email address: pierre.lavoie@polymtl.ca (Pierre Lavoie)

in a preliminary phase. This icing suite uses an Euler flow solver combined with an integral boundary layer code. Thus, the objective is to apply an immersed boundary method to the Euler equations.

From the literature, a variety of Immersed Boundary Methods are available, ranging from the geometric Cut-Cell approach [3, 4, 5] to discrete [6, 7, 8] and continuous methods [9, 10]. Here the goal is not to perform a detailed and comprehensive comparison between the different methods, instead the reader is referred to [11, 12] for a thorough review.

Continuous immersed boundary methods have the advantage of being independent of the discretization and numerical methods. Furthermore, continuous approaches such as the penalization method of [10] are appealing for their simplicity of implementation. The penalization method was applied to incompressible Navier-Stokes equations [13, 14, 10, 15, 16] and extended to compressible flows [17, 18, 19, 20, 21, 22, 23]. However, only one application of the Penalization method to the Euler equation was found in the literature [24] by using the method described in [23].

In this paper, the Characteristic-Based Volume Penalization (CBVP) of [23, 24] is applied to the Euler equation in an alternative way. Our approach uses a different set of boundary conditions inspired by [25] where the conservation of entropy and total enthalpy in the normal direction are applied. Additionally, artificial dissipation terms present in the original CBVP method are removed in favor of convective terms. This is more suitable for the Euler equations as routines for the computation of dissipation terms are not always readily available for this type of solvers.

This paper is divided in six sections. Excluding this introduction section, the paper starts with the review of two types of numerical wall boundary conditions for the Euler equations and their application to body-fitted meshes in a finite volume context. This is helpful to understand what is applied for the immersed boundary method. Then in section 3, the representation of the immersed boundary is discussed. Section 4 is dedicated to the description of the penalization method. More precisely, the penalization method of [23] and its application to the Euler equations [24] is discussed. Then the development of the new penalization method is presented along with implementation details for a Finite Volume Method. In section 5, verification of the new method is made on canonical test cases and on a challenging 2D ice horn case. Some comparisons are also made against the CBVP method. Section 6 concludes on the new penalization method.

2. Wall Boundary Conditions for the Euler Equations

In this section, wall boundary conditions for the Euler equations are reviewed for body-fitted meshes. The Euler equations are reminded in both conservative and non-conservative forms as both formulations are used later in

this paper. Then two types of numerical wall boundary conditions are described for finite volume implementation. The non-conservative form of the Euler equations is:

$$\begin{aligned} \frac{\partial \rho}{\partial t} + \rho \nabla \cdot \mathbf{v} + \mathbf{v} \cdot \nabla \rho &= 0 \\ \rho \frac{\partial \mathbf{v}}{\partial t} + \rho \mathbf{v} \cdot \nabla \mathbf{v} + \nabla P &= 0 \\ \rho \frac{\partial e}{\partial t} + \rho \mathbf{v} \cdot \nabla e + P \nabla \cdot \mathbf{v} &= 0 \end{aligned} \quad (1)$$

and its conservative form is written as:

$$\begin{aligned} \frac{\partial \rho}{\partial t} + \nabla \cdot (\rho \mathbf{v}) &= 0 \\ \frac{\partial (\rho \mathbf{v})}{\partial t} + \nabla \cdot (\rho \mathbf{v} \otimes \mathbf{v} + P \mathbf{I}) &= 0 \\ \frac{\partial (\rho E)}{\partial t} + \nabla \cdot ((\rho E + P) \mathbf{v}) &= 0 \end{aligned} \quad (2)$$

where ρ is the density, \mathbf{v} the velocity, P the pressure, e the internal energy, E the total energy and \mathbf{I} the identity tensor. The system is closed using the ideal gas law.

$$e = \frac{R}{\gamma - 1} T \quad (3)$$

$$E = e + \frac{1}{2} \|\mathbf{v}\|^2 \quad (4)$$

$$P = \rho R T \quad (5)$$

The specific gas constant for air is $R = 287.0$ and the specific heat ratio is $\gamma = 1.4$.

The wall boundary conditions for the Euler equations are set in order to obtain a no-penetration velocity (or slip velocity) where $\mathbf{v} \cdot \mathbf{n} = 0$. This leads to the following wall flux (in 2D):

$$\mathbf{F}_{wall} = \begin{bmatrix} \rho \mathbf{v} \cdot \mathbf{n} \\ \rho u \mathbf{v} \cdot \mathbf{n} + P n_x \\ \rho v \mathbf{v} \cdot \mathbf{n} + P n_y \\ \rho H \mathbf{v} \cdot \mathbf{n} \end{bmatrix} = \begin{bmatrix} 0 \\ P n_x \\ P n_y \\ 0 \end{bmatrix} \quad (6)$$

On a physics point of view, only the no-penetration velocity is a required boundary condition at the wall. However on a numerical point of view (i.e. finite volume method), adequate values for the primitive variables (ρ , u , v and P) are required in the ghost cells for both the evaluation of the wall flux and the evaluation of the gradients. Two approaches are reviewed here, which are both implemented in the unstructured Euler flow solver of IGLOO2D: the Symmetry Technique (ST) and the Curvature Corrected Symmetry Technique (CCST).

2.1. Symmetry Technique (ST)

Considering a Finite Volume cell-centered discretization using ghost-cells at the wall boundary (Figure 1), the Symmetry Technique consists in imposing the following

primitive variables in the ghost cells (g) to obtain the appropriate wall flux:

$$\mathbf{v}_g = \mathbf{v}_d - 2(\mathbf{v}_d \cdot \mathbf{n})\mathbf{n} \quad (7)$$

$$\rho_g = \rho_d \quad (8)$$

$$P_g = P_d \quad (9)$$

where \mathbf{n} is the wall normal. It follows the assumption that the wall is locally flat (negligible curvature). This assumption holds if the mesh in the vicinity of the wall is sufficiently refined (see Eq. (11) with $\Delta n = 0$).

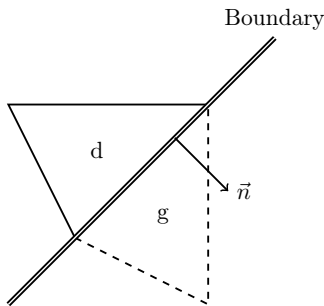


Figure 1: Representation of the domain (d) and ghost (g) cells at the boundary along with the wall normal (\mathbf{n})

2.2. Curvature Corrected Symmetry Technique (CCST)

The CCST is presented in 2D in [25, 26], then extended to 3D in [27] and applied to 2D unstructured meshes in [28]. This approach imposes the normal momentum relation to account for the wall curvature in the pressure extrapolation, which can be written as:

$$\left. \frac{\partial P}{\partial \mathbf{n}} \right|_w = \rho_w \kappa \|\mathbf{v}_w\|^2 \quad (10)$$

where κ is the signed wall curvature (positive if the center of curvature is on the domain/fluid side, negative on the ghost/solid side). Note that Eq. (10) is derived from the momentum equation and is valid for both steady and unsteady flows. However its application is limited to stationary and non-deformable bodies ($\frac{\partial \mathbf{n}}{\partial t} = 0$). As a consequence of Eq. (10) the ghost cell values are computed as:

$$P_g = P_d + \rho_w \kappa \|\mathbf{v}_w\|^2 \Delta n \quad (11)$$

$$\rho_g = \rho_d \left(\frac{P_g}{P_d} \right)^{1/\gamma} \quad (12)$$

$$(\mathbf{v} \cdot \mathbf{n})_g = -(\mathbf{v} \cdot \mathbf{n})_d \quad (13)$$

$$(\mathbf{v} \cdot \mathbf{t})_g^2 = (\mathbf{v} \cdot \mathbf{t})_d^2 + \frac{2\gamma}{\gamma-1} \left(\frac{P_d}{\rho_d} - \frac{P_g}{\rho_g} \right) \quad (14)$$

where Δn is the distance between the centers of the domain (d) and ghost (g) cells along the normal direction. Eq. (12) and Eq. (14) result from the conservation of entropy and total enthalpy respectively. The wall (w) values in Eq. (11)

are typically taken as [25, 28]:

$$\rho_w = \rho_d \quad (15)$$

$$\mathbf{v}_w = \mathbf{v}_d - (\mathbf{v}_d \cdot \mathbf{n})\mathbf{n} \quad (16)$$

The norm of the tangential velocity is computed from Eq. (14) and its direction follows the unit tangent vector computed as:

$$\mathbf{t} = \frac{\mathbf{v} - (\mathbf{v} \cdot \mathbf{n})\mathbf{n}}{\|\mathbf{v} - (\mathbf{v} \cdot \mathbf{n})\mathbf{n}\|} \quad (17)$$

When the wall curvature is not negligible, the CCST is shown to be more accurate and to exhibit faster grid convergence [25] for steady flow computations. The ST and CCST boundary conditions converge towards the same solution as the mesh is refined. Furthermore, when the curvature is zero ($\kappa = 0$), the CCST method simplifies to the ST approach.

3. Immersed Boundary Representation

Before describing the penalization methods for the Euler equations, it is worth discussing how the immersed boundary is represented.

3.1. Signed Distance

For this paper, the immersed boundary is defined by a discrete list of nodes (2D). The location of the immersed boundary is defined by the level-set $\phi = 0$, where ϕ is the signed distance field from the immersed boundary. Values of ϕ are computed using a geometric approach: evaluating the minimum projected distance to the edges forming the immersed boundary [29].

The sign of ϕ is determined by a ray casting algorithm [29] where the immersed boundary is considered as a closed body. To reduce computation costs a bounding box is created around the body of interest by identifying \mathbf{x}_{min} and \mathbf{x}_{max} of the discrete node list. The cell centers outside this bounding box have a positive sign ($\phi > 0$, fluid). For the cell centers inside the bounding box, the ray casting algorithm is applied.

Using a signed distance field leads to a simple evaluation of the normals (\mathbf{n}_ϕ) and curvature (κ) of the immersed boundary using:

$$\mathbf{n}_\phi = -\frac{\nabla \phi}{\|\nabla \phi\|} \quad (18)$$

$$\kappa = \nabla \cdot \mathbf{n}_\phi. \quad (19)$$

Note that the normal based on ϕ has a negative sign in order to point towards the solid zone ($\phi < 0$). This is useful in the definition of the Penalization methods presented in the next section.

3.2. Data Extraction

To extract the data at the immersed boundary (e.g. density, velocity, pressure), a simple weighted least square interpolation at the discrete nodes defining the immersed boundary is used. The interpolation stencil is determined firstly by identifying the cell containing the immersed boundary node, and secondly by saving the extended neighborhood of this cell. The penalization methods described in the following sections extend the fluid data into the solid zone (from outside the geometry to its inside). Thus the interpolation stencil in the vicinity of the solid/fluid interface is assumed to be filled with valid data to perform the interpolation.

4. Penalization Method

In this section, the classical Volume Penalization method is presented along with a discussion on its application to the Euler equations. Then the penalization method of [23] (CBVP) is described followed by the development of the improved penalization approach called CBVP-Hs because it conserves total enthalpy (H) and entropy (s).

4.1. Volume Penalization

The Volume Penalization method consists in adding source terms in the continuous form of the equation to enforce the desired boundary condition. The source terms are activated/deactivated using a mask function (χ) equal to unity in the solid and zero in the fluid. In this way, only the solid is penalized and the usual equations are retrieved in the fluid. The penalization parameter ($\eta \ll 1$) ensures the boundary condition is enforced accurately. This type of method is well suited for the imposition of Dirichlet boundary conditions for moving or stationary bodies. The volume penalization is known to be 0^{th} order accurate in the imposition of the boundary condition, meaning a global 1^{st} order accuracy in space can be achieved.

In order to review how boundary conditions are imposed using the Volume Penalization, it is applied to a generic partial differential equation (PDE):

$$\frac{\partial u}{\partial t} = RHS. \quad (20)$$

This equation is solved on a generic computational domain Ω including an immersed solid domain Ω_s , where the fluid domain is $\Omega_f = \Omega \setminus \Omega_s$. To impose a Dirichlet condition $u = u_{bc}$ on the fluid/solid interface, a source term is applied to the generic PDE as:

$$\frac{\partial u}{\partial t} = RHS - \frac{\chi}{\eta}(u - \tilde{u}_{bc}(\mathbf{x}, t)) \quad (21)$$

where the physical RHS is solved both in the fluid and the solid. The scalar field u is penalized in the solid in order to impose u_{bc} . Here \tilde{u}_{bc} is an extension of u_{bc} on Ω_s .

When solving Eq. (21) in the solid, η is selected to be small enough for the *RHS* to be considered negligible in

front of the penalization term. It comes back to solving an ordinary differential equation of the form:

$$\frac{du}{dt} = -\frac{1}{\eta}(u - \tilde{u}_{bc}) \quad (22)$$

The solution of this ODE is a rapidly decaying exponential, meaning $u = u_{bc}$ is imposed almost instantaneously:

$$|(u - \tilde{u}_{bc})| = A_0 e^{-t/\eta} \quad (23)$$

The penalization parameter η can be seen as a characteristic timescale which must be small ($\eta \ll 1$) in order to enforce the boundary condition.

4.1.1. Application to the Euler Equations

The volume penalization is widely used for the Navier-Stokes equations where the velocity \mathbf{v} is penalized on the momentum equations to obtain $\mathbf{v} = 0$ in the solid (for a stationary body). A simple adaptation of this approach to the Euler equations consists in penalizing the momentum equations to obtain $\mathbf{v} \cdot \mathbf{n} = 0$ in the solid instead, similar to [30]. In brief, the goal is to obtain a slip velocity in the solid instead of the no-slip condition. In non-conservative form the penalized Euler equations read:

$$\begin{aligned} \frac{\partial \rho}{\partial t} + \nabla \cdot (\rho \mathbf{v}) &= 0 \\ \rho \frac{\partial \mathbf{v}}{\partial t} + \rho \mathbf{v} \cdot \nabla \mathbf{v} + \nabla P &= -\frac{\chi}{\eta} \rho (\mathbf{v} \cdot \mathbf{n}_\phi) \mathbf{n}_\phi \\ \rho \frac{\partial e}{\partial t} + \rho \mathbf{v} \cdot \nabla e + P \nabla \cdot \mathbf{v} &= 0 \end{aligned} \quad (24)$$

In the fluid ($\chi = 0$) the usual Euler equations are retrieved. In the solid ($\chi = 1$), by identifying terms of same order of magnitude, the no-penetration velocity is enforced:

$$\rho (\mathbf{v} \cdot \mathbf{n}_\phi) \mathbf{n}_\phi = 0 \quad (25)$$

The Euler equations are also solved in the solid but because of Eq. (25), only the tangential component of the velocity remains (\mathbf{v}_t):

$$\begin{aligned} \frac{\partial \rho}{\partial t} + \nabla \cdot (\rho \mathbf{v}_t) &= 0 \\ \rho \frac{\partial \mathbf{v}_t}{\partial t} + \rho \mathbf{v}_t \cdot \nabla \mathbf{v}_t + \nabla P &= 0 \\ \rho \frac{\partial e}{\partial t} + \rho \mathbf{v}_t \cdot \nabla e + P \nabla \cdot \mathbf{v}_t &= 0 \end{aligned} \quad (26)$$

Contrary to the Navier-Stokes equations where the fluid is at rest at the immersed boundary and in the solid (no-slip wall), Eq. (26) shows that there is an actual fluid flow in the solid with the Euler equations (slip wall). Furthermore, as the no-penetration velocity is imposed at the immersed boundary, there is a lack of communication from the fluid to the solid. One constraint only is imposed: the immersed boundary is a streamline because it is parallel to the flow. But some discontinuities in tangential velocity (\mathbf{v}_t), pressure, entropy and total enthalpy are allowed

across the immersed boundary, which is thus a slip line. The objective is to retrieve continuity across the streamline at the immersed boundary by the imposition of additional constraints in the normal direction. This can be achieved by enforcing Neumann boundary conditions, which can be implemented using the penalization method of [23], presented in the following section.

4.2. Characteristic-Based Volume Penalization (CBVP)

The Characteristic-based Volume Penalization (CBVP) method [23] provides a systematic way of implementing Dirichlet, Neumann and Robin boundary conditions by the addition of hyperbolic penalization terms. It uses a sharp Heaviside function for the mask (χ) where $\chi = 1$ in the solid (Ω_s) and $\chi = 0$ in the fluid (Ω_f). This leads to a staircase definition of the immersed boundary (IB) as shown in Figure 2. However, a smooth solution is recovered at the IB by the use of hyperbolic penalization terms for Neumann and Robin conditions, and by the use of dissipation terms for Dirichlet conditions. This makes for a more flexible penalization method than the classic volume penalization.

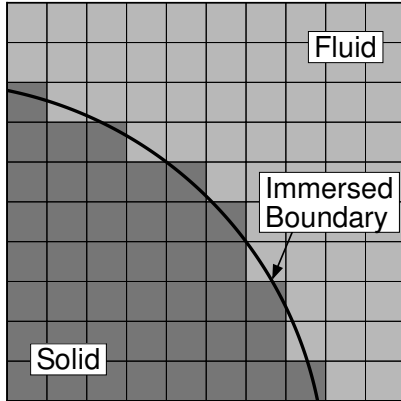


Figure 2: Staircase representation of the solid

In the following sections, the boundary conditions as imposed by [23, 24] are applied on the generic PDE (Eq. (20)) and then to the Euler equations.

4.2.1. Dirichlet Boundary Condition

The Dirichlet condition $u = u_{bc}$ is imposed on the generic PDE as:

$$\frac{\partial u}{\partial t} = (1 - \chi)RHS - \frac{\chi}{\eta}(u - \tilde{u}_{bc}(\mathbf{x}, t)) + \chi\nu_\eta \nabla^2 u \quad (27)$$

As with the Volume Penalization, the mask function χ activates the penalization terms in the solid only. In the fluid, the mask function is zero and therefore the generic PDE is retrieved.

As explained in [23], for the CBVP method the *RHS* is removed from Ω_s to prevent any interaction with the penalization terms. The removal of the *RHS* also disables

any physical dissipation/viscosity. As a replacement, an artificial dissipation term is added using the artificial viscosity ν_η which must be of the order $\nu_\eta \geq \Delta x^2/\eta$. According to [23], this term helps in retrieving a smooth solution at the immersed boundary for Dirichlet conditions

4.2.2. Neumann Boundary Condition

The Neumann condition $\mathbf{n} \cdot \nabla u = q$ is imposed by the addition of a hyperbolic penalization term:

$$\frac{\partial u}{\partial t} = (1 - \chi)RHS - \frac{\chi}{\eta_c}(\mathbf{n}_\phi \cdot \nabla u - q(\mathbf{x}, t)) \quad (28)$$

where \mathbf{n}_ϕ is the normal to the immersed boundary pointing towards the solid. Note that $1/\eta_c$ can be seen as a characteristic velocity with $\eta_c \ll 1$. In the solid ($\chi = 1$), the equation reduces to pure convection, propagating the information from the fluid to the solid in a direction normal to the immersed boundary. A similar approach is applied for Robin conditions [23].

4.2.3. Application to the Euler equations

In [24], a set of penalized Euler equations are presented very briefly. In non-conservative form, it writes:

$$\begin{aligned} \frac{\partial \rho}{\partial t} + (1 - \chi)\nabla \cdot (\rho \mathbf{v}) &= -\frac{\chi}{\eta_c} \left(\mathbf{n}_\phi \cdot \nabla \rho - \kappa \frac{\rho^2}{P} \|\mathbf{v}\|^2 \right) \\ \rho \frac{\partial \mathbf{v}}{\partial t} + (1 - \chi)(\rho \mathbf{v} \cdot \nabla \mathbf{v} + \nabla P) &= -\frac{\chi}{\eta} \rho (\mathbf{v} \cdot \mathbf{n}_\phi) \mathbf{n}_\phi + \chi \rho \nu_\eta \nabla^2 \mathbf{v} \\ \rho \frac{\partial e}{\partial t} + (1 - \chi)(\rho \mathbf{v} \cdot \nabla e + P \nabla \cdot \mathbf{v}) &= -\frac{\chi}{\eta_c} (\rho \mathbf{n}_\phi \cdot \nabla e) \end{aligned} \quad (29)$$

In the fluid ($\chi = 0$) the usual Euler equations are retrieved. In the solid ($\chi = 1$), by identifying terms of the same order of magnitude, the following conditions are enforced:

$$\mathbf{n}_\phi \cdot \nabla \rho = \kappa \frac{\rho^2}{P} \|\mathbf{v}\|^2 \quad (30)$$

$$-\frac{1}{\eta} \rho (\mathbf{v} \cdot \mathbf{n}_\phi) \mathbf{n}_\phi + \nu_\eta \nabla^2 \mathbf{v} = 0 \quad (31)$$

$$\mathbf{n}_\phi \cdot \nabla e = 0 \quad (32)$$

This set of equations is equivalent to imposing an adiabatic wall (Eq. (32)), a no penetration velocity (Eq. (31)) and the normal momentum relation which relates the pressure gradient to the wall curvature (Eq. (30)), except it is written in terms of the density gradient instead. The normal momentum relation can be written as:

$$\mathbf{n}_\phi \cdot \nabla P = \kappa \rho \|\mathbf{v}\|^2 \quad (33)$$

where in 2D, the curvature (κ) is computed from the normals to the immersed boundary \mathbf{n}_ϕ as $\kappa = \nabla \cdot \mathbf{n}_\phi$. To obtain Eq. (30), one must use the ideal gas law ($P = \rho e(\gamma - 1)$) in combination with the normal momentum relation (Eq. (33)) and apply the adiabatic wall condition ($\mathbf{n}_\phi \cdot \nabla e = 0$).

The dissipation term in Eq. (31) helps in obtaining continuity of the tangential velocity but also hinders the correct imposition of $(\mathbf{v} \cdot \mathbf{n})\mathbf{n} = 0$. Thus this parameter must be selected small enough for the correct imposition of the no-penetration velocity, but large enough to ensure continuity and stability. In this paper the dissipation parameter is taken as $\nu_\eta = \Delta x^2/\eta$ as suggested in [23]. Note that this penalization method depends on three parameters requiring adjustments: η , η_c and ν_η instead of one for the classic volume penalization method.

4.3. CBVP-Hs

Because of the dissipation term in the CBVP method, there is a smooth transition of the velocity from the fluid to the solid. However, this transition is not based on the physics of the problem. Furthermore, for Euler flow solvers, routines are not always readily available to compute dissipation terms. It is thus more convenient to avoid them if possible. For these reasons, a new method inspired by the CBVP of [23] is proposed hereafter.

The goal is to develop a method that would respect the properties of the inviscid ideal gas flow in the vicinity of the wall streamline. The streamline is, of course, defined by the no-penetration velocity (Eq. (37)). The continuity of tangential velocity, pressure, entropy and total enthalpy must be ensured by additional equations. The normal momentum relation (Eq. (33)) allows the continuity of pressure. The normal conservation of total enthalpy (Eq. (34)) and the normal conservation of entropy (Eq. (35)) are imposed to close the system:

$$\mathbf{n}_\phi \cdot \nabla H = 0 \quad (34)$$

$$\mathbf{n}_\phi \cdot \nabla s = 0 \quad (35)$$

$$\mathbf{n}_\phi \cdot \nabla P = \kappa \rho \|\mathbf{v}\|^2 \quad (36)$$

$$(\mathbf{v} \cdot \mathbf{n}_\phi)\mathbf{n}_\phi = 0 \quad (37)$$

where \mathbf{n}_ϕ is the normal to the immersed boundary based on the signed distance field (ϕ). This set of boundary conditions allows the continuity of the flow variables including the norm of the velocity across the boundary. It is better suited for homentropic and homenthalpic flows which are the primary target of our model, although the presence of a shock wave for instance may not hinder the use of (Eq. (35)) as long as the shock is parallel to \mathbf{n}_ϕ .

This new method can be seen as a first order implementation of the CCST boundary condition of [25, 26, 27] using the CBVP method of [23]. Because it is based on the CBVP but designed to conserve the entropy (s) and total enthalpy (H), it is referred to as CBVP-Hs. It is important to understand that the only physical wall boundary condition required for the Euler equations is the no-penetration velocity. The other conditions are numerical (normal momentum relation, conservation of total enthalpy and entropy) and are used to improve the accuracy of the model, the continuity of the solution near the immersed boundary and provide adequate support for the evaluation of the

fluxes and gradients. They also make the interpolation of wall data easier.

In the following sections, penalization terms are first derived for the primitive variables and applied to the non-conservative form of the Euler equations. It is useful to start with the primitive variables as the penalization terms can easily be derived for them. Then the transition from the non-conservative to the conservative form naturally provides the penalized Euler equations in terms of conservative variables.

4.3.1. Penalization of the Primitive Variables

In this section, penalization terms are derived for the non-conservative form of the Euler equations (Eq. (1)). Hyperbolic penalization terms of the form $\mathbf{n} \cdot \nabla u = q$ are sought, where u is ρ, \mathbf{v} or e .

The penalization term for the density is derived from Eqs. (35)–(33). The conservation of entropy can be written as:

$$\mathbf{n}_\phi \cdot \nabla s = \mathbf{n}_\phi \cdot \nabla \left(\frac{P}{\rho^\gamma} \right) = 0 \quad (38)$$

$$\Rightarrow \mathbf{n}_\phi \cdot \nabla \rho = \frac{\rho}{\gamma P} \mathbf{n}_\phi \cdot \nabla P \quad (39)$$

By substituting the normal momentum relation (Eq. (33)) in Eq. (39), a relation for the normal density gradient is obtained. It is applied to the continuity equation as a hyperbolic penalization term (Eq. (40)).

$$\frac{\chi}{\eta_c} \left(\mathbf{n}_\phi \cdot \nabla \rho - \frac{\rho^2}{\gamma P} \kappa \|\mathbf{v}\|^2 \right) = 0 \quad (40)$$

A penalization term for the internal energy can be derived from equations (5), (3) and (39), which gives:

$$\frac{\chi}{\eta_c} \left(\mathbf{n}_\phi \cdot \nabla e - \frac{1}{\gamma} \kappa \|\mathbf{v}\|^2 \right) = 0 \quad (41)$$

At this point, only the penalization term on velocity is missing. This term is the application of the no-penetration velocity (Eq. (37)) as a Dirichlet condition and a hyperbolic penalization term denoted $\mathcal{P}_\mathbf{v}$ which must be determined to set the velocity magnitude.

$$\rho \frac{\partial \mathbf{v}}{\partial t} + (1 - \chi)(\rho \mathbf{v} \cdot \nabla \mathbf{v} + \nabla P) = \mathcal{P}_\mathbf{v} - \frac{\chi}{\eta} \rho (\mathbf{v} \cdot \mathbf{n}_\phi) \mathbf{n}_\phi \quad (42)$$

In addition, the conservation of total enthalpy must still be enforced. The term $\mathcal{P}_\mathbf{v}$ can thus be derived in two steps. First, by using the normal conservation of total enthalpy (Eq. (34)) one can derive a condition on kinetic energy. The conservation of total enthalpy ($\mathbf{n}_\phi \cdot \nabla H = 0$) can be written as:

$$\frac{\gamma}{\gamma - 1} \mathbf{n}_\phi \cdot \nabla \left(\frac{P}{\rho} \right) + \mathbf{n}_\phi \cdot \nabla \left(\frac{1}{2} \|\mathbf{v}\|^2 \right) = 0 \quad (43)$$

with

$$\mathbf{n}_\phi \cdot \nabla \left(\frac{P}{\rho} \right) = \frac{\mathbf{n}_\phi}{\rho} \cdot \nabla P - \frac{P \mathbf{n}_\phi}{\rho^2} \cdot \nabla \rho \quad (44)$$

By using Eq. (44), the normal momentum relation (Eq. (33)) and the condition on density (Eq. (40)), the condition on kinetic energy is retrieved.

$$\Rightarrow \mathbf{n}_\phi \cdot \nabla \left(\frac{1}{2} \|\mathbf{v}\|^2 \right) + \kappa \|\mathbf{v}\|^2 = 0 \quad (45)$$

It can also be recast in a penalized equation for the kinetic energy in the solid:

$$\rho \frac{\partial \left(\frac{1}{2} \|\mathbf{v}\|^2 \right)}{\partial t} = -\frac{\chi}{\eta_c} \left(\rho \mathbf{n}_\phi \cdot \nabla \left(\frac{1}{2} \|\mathbf{v}\|^2 \right) + \rho \kappa \|\mathbf{v}\|^2 \right) \quad (46)$$

Second, a relation for kinetic energy can also be computed from the momentum equation (42) scalar product with \mathbf{v} as:

$$\begin{aligned} \mathbf{v} \cdot \rho \frac{\partial \mathbf{v}}{\partial t} + \mathbf{v} \cdot (1 - \chi)(\rho \mathbf{v} \cdot \nabla \mathbf{v} + \nabla P) = \\ \mathbf{v} \cdot \mathcal{P}_\mathbf{v} - \mathbf{v} \cdot \frac{\chi}{\eta} \rho (\mathbf{v} \cdot \mathbf{n}_\phi) \mathbf{n}_\phi \end{aligned} \quad (47)$$

By considering this equation in the solid ($\chi = 1$) and by keeping only terms of the same order of magnitude, it reads:

$$\mathbf{v} \cdot \rho \frac{\partial \mathbf{v}}{\partial t} = \mathbf{v} \cdot \mathcal{P}_\mathbf{v} \quad (48)$$

or

$$\rho \frac{\partial \left(\frac{1}{2} \|\mathbf{v}\|^2 \right)}{\partial t} = \mathbf{v} \cdot \mathcal{P}_\mathbf{v} \quad (49)$$

This simplification follows the assumption that η and η_c are not of the same order of magnitude and thus, that $\mathbf{v} \cdot \mathbf{n}_\phi$ exponentially tend towards zero. By equating, Eq. (49) and Eq. (46), it leads to:

$$\mathbf{v} \cdot \mathcal{P}_\mathbf{v} = -\frac{\chi}{\eta_c} \left(\rho \mathbf{n}_\phi \cdot \nabla \left(\frac{1}{2} \|\mathbf{v}\|^2 \right) + \rho \kappa \|\mathbf{v}\|^2 \right) \quad (50)$$

$\mathcal{P}_\mathbf{v}$ must be selected to respect this condition on kinetic energy (Eq. (50)). A natural approach is to select $\mathcal{P}_\mathbf{v}$ orthogonal to \mathbf{n} in order to decouple the hyperbolic penalization term and the Dirichlet condition (see Eq. (42)). However, no practical formulation was found for use with the Finite Volume Method. An alternative and simpler choice for $\mathcal{P}_\mathbf{v}$ is:

$$\mathcal{P}_\mathbf{v} = -\frac{\chi}{\eta_c} (\rho \mathbf{n}_\phi \cdot \nabla \mathbf{v} + \kappa \rho \mathbf{v}) \quad (51)$$

In Eq. (51), the hyperbolic penalization term and the Dirichlet condition in Eq. (42) are decoupled by using $\eta \ll \eta_c$.

The non-conservative form of the penalized equations can now be updated using the hyperbolic terms for ρ , \mathbf{v} and e :

$$\begin{aligned} \frac{\partial \rho}{\partial t} + (1 - \chi) \nabla \cdot (\rho \mathbf{v}) &= -\frac{\chi}{\eta_c} \left(\mathbf{n}_\phi \cdot \nabla \rho - \kappa \frac{\rho^2}{\gamma P} \|\mathbf{v}\|^2 \right) \\ \rho \frac{\partial \mathbf{v}}{\partial t} + (1 - \chi)(\rho \mathbf{v} \cdot \nabla \mathbf{v} + \nabla P) &= -\frac{\chi}{\eta_c} (\rho \mathbf{n}_\phi \cdot \nabla \mathbf{v} + \kappa \rho \mathbf{v}) \\ &\quad - \frac{\chi}{\eta} \rho (\mathbf{v} \cdot \mathbf{n}_\phi) \mathbf{n}_\phi \\ \rho \frac{\partial e}{\partial t} + (1 - \chi)(\rho \mathbf{v} \cdot \nabla e + P \nabla \cdot \mathbf{v}) &= -\frac{\chi}{\eta_c} \left(\rho \mathbf{n}_\phi \cdot \nabla e - \kappa \frac{\rho}{\gamma} \|\mathbf{v}\|^2 \right) \end{aligned} \quad (52)$$

4.3.2. Penalization of the Conservative Variables

By transferring to the conservative form, the equations including the penalization terms become:

$$\begin{aligned} \frac{\partial \rho}{\partial t} + (1 - \chi) \nabla \cdot (\rho \mathbf{v}) &= -\frac{\chi}{\eta_c} \left(\mathbf{n}_\phi \cdot \nabla \rho - \kappa \frac{\rho^2}{\gamma P} \|\mathbf{v}\|^2 \right) \\ \frac{\partial \rho \mathbf{v}}{\partial t} + (1 - \chi) \nabla \cdot (\rho \mathbf{v} \otimes \mathbf{v} + P \mathbf{I}) &= -\frac{\chi}{\eta} \rho (\mathbf{v} \cdot \mathbf{n}_\phi) \mathbf{n}_\phi \\ &\quad - \frac{\chi}{\eta_c} \left(\mathbf{n}_\phi \cdot \nabla (\rho \mathbf{v}) + \kappa \rho \mathbf{v} \left(1 - \frac{\rho}{\gamma P} \|\mathbf{v}\|^2 \right) \right) \\ \frac{\partial \rho E}{\partial t} + (1 - \chi) \nabla \cdot ((\rho E + P) \mathbf{v}) &= -\frac{\chi}{\eta} \rho (\mathbf{v} \cdot \mathbf{n}_\phi)^2 \\ &\quad - \frac{\chi}{\eta_c} \left(\rho \mathbf{n}_\phi \cdot \nabla E - \frac{(\gamma - 1)}{\gamma} \rho \kappa \|\mathbf{v}\|^2 \right) \end{aligned} \quad (53)$$

The energy equation can also be written as:

$$\begin{aligned} \frac{\partial \rho E}{\partial t} + (1 - \chi) \nabla \cdot ((\rho E + P) \mathbf{v}) &= -\frac{\chi}{\eta} \rho (\mathbf{v} \cdot \mathbf{n}_\phi)^2 \\ &\quad - \frac{\chi}{\eta_c} \rho \mathbf{n}_\phi \cdot \nabla H \end{aligned} \quad (54)$$

Using this set of penalization terms ensure Eqs. (34)–(37) are respected. Furthermore, the term $\mathcal{P}_\mathbf{v}$ replace the dissipation term employed in [23] on the momentum equation. This convection term is derived from physical arguments in order to respect the conservation of total enthalpy instead of using a numerical artifice.

4.3.3. Implementation Details

The penalized Euler equations of Eq. (53) are implemented in a cell-centered Finite Volume framework using unstructured meshes. They are written in vector form as:

$$\frac{\partial \mathbf{W}}{\partial t} + (1 - \chi) \nabla \cdot \mathbf{F}_{Euler} = -\chi \nabla \cdot \mathbf{F}_{ibm} + \chi \mathbf{S}_{ibm} \quad (55)$$

where the penalization terms are conveniently split into flux (\mathbf{F}_{ibm}) and source (\mathbf{S}_{ibm}) terms.

$$\mathbf{W} = \begin{bmatrix} \rho \\ \rho u \\ \rho v \\ \rho E \end{bmatrix}, \quad \mathbf{F}_{Euler} = \begin{bmatrix} \rho \mathbf{v} \\ \rho u \mathbf{v} + P_x \\ \rho v \mathbf{v} + P_y \\ \rho H \mathbf{v} \end{bmatrix} \quad (56)$$

$$\mathbf{F}_{ibm} = \frac{1}{\eta_c} \begin{bmatrix} \rho \mathbf{n}_\phi \\ \rho u \mathbf{n}_\phi \\ \rho v \mathbf{n}_\phi \\ \rho H \mathbf{n}_\phi \end{bmatrix} \quad (57)$$

The immersed boundary source term (\mathbf{S}_{ibm}) is split in Dirichlet, convective and curvature contributions:

$$\mathbf{S}_{ibm} = \mathbf{S}_{ibm,D} + \mathbf{S}_{ibm,conv} + \mathbf{S}_{ibm,curv} \quad (58)$$

$$\mathbf{S}_{ibm,D} = \frac{1}{\eta} \begin{bmatrix} 0 \\ -\rho(\mathbf{v} \cdot \mathbf{n}_\phi) n_{\phi,x} \\ -\rho(\mathbf{v} \cdot \mathbf{n}_\phi) n_{\phi,y} \\ -\rho(\mathbf{v} \cdot \mathbf{n}_\phi)^2 \end{bmatrix} \quad (59)$$

$$\mathbf{S}_{ibm,conv} = \frac{1}{\eta_c} \begin{bmatrix} \rho \nabla \cdot \mathbf{n}_\phi \\ \rho u \nabla \cdot \mathbf{n}_\phi \\ \rho v \nabla \cdot \mathbf{n}_\phi \\ \rho H \nabla \cdot \mathbf{n}_\phi \end{bmatrix} \quad (60)$$

$$\mathbf{S}_{ibm,curv} = \frac{1}{\eta_c} \kappa \begin{bmatrix} \rho \frac{\rho}{\gamma P} \|\mathbf{v}\|^2 \\ \rho u \left(\frac{\rho}{\gamma P} \|\mathbf{v}\|^2 - 1 \right) \\ \rho v \left(\frac{\rho}{\gamma P} \|\mathbf{v}\|^2 - 1 \right) \\ \rho H \frac{\rho}{\gamma P} \|\mathbf{v}\|^2 \end{bmatrix} \quad (61)$$

where the convective source term $\mathbf{S}_{ibm,conv}$ comes from rewriting Eq. (53) to isolate \mathbf{F}_{ibm} . From the immersed boundary flux (Eq. (57)), the system is shown to be hyperbolic in the solid with eigenvalues \mathbf{n}_ϕ , \mathbf{n}_ϕ , \mathbf{n}_ϕ and $\gamma \mathbf{n}_\phi$.

The penalization of the Euler equations leads to a stiff system as the penalization parameters (η and η_c) are very small. One way to alleviate this problem is to solve the system implicitly. In this paper it is solved using a BICGSTAB algorithm with a block Jacobi preconditioner. The Euler fluxes are computed by a 2^{nd} order Roe scheme while the immersed boundary fluxes are evaluated with a simple 1^{st} order upwind scheme (upwinded by \mathbf{n}_ϕ).

The mask function χ is the Heaviside function (\mathcal{H}) based on the signed distance field ϕ .

$$\chi = \mathcal{H}(-\phi) \quad (62)$$

The level-set $\phi = 0$ determines the location of the immersed boundary while $\phi < 0$ in the solid and $\phi > 0$ in the fluid. It can be seen that in the fluid ($\chi = 0$), the usual Euler equations are retrieved while in the solid ($\chi = 1$) only the penalization terms are activated.

From [23], $\eta_c \ll 1$ and $\eta \ll 1$ in order to enforce the correct condition in the solid by penalization. In the current

implementation, a slightly different approach is followed. Since the Euler fluxes are deactivated in the solid, η_c is not required to be very small in order to propagate the fluid properties towards the solid. Here, the immersed boundary fluxes are not penalized but are merely a replacement for the Euler fluxes inside the solid. It comes back to solving propagation equations in the solid, which are penalized to apply the no-penetration velocity. By using $\eta_c = 1$, the equations in the solid are:

$$\begin{aligned} \frac{\partial \rho}{\partial t} + \mathbf{n}_\phi \cdot \nabla \rho &= \kappa \frac{\rho^2}{\gamma P} \|\mathbf{v}\|^2 \\ \frac{\partial \rho \mathbf{v}}{\partial t} + \mathbf{n}_\phi \cdot \nabla (\rho \mathbf{v}) &= \kappa \rho \mathbf{v} \left(\frac{\rho}{\gamma P} \|\mathbf{v}\|^2 - 1 \right) - \frac{1}{\eta} \rho (\mathbf{v} \cdot \mathbf{n}_\phi) \mathbf{n}_\phi \\ \frac{\partial \rho E}{\partial t} + \rho \mathbf{n}_\phi \cdot \nabla H &= -\frac{1}{\eta} \rho (\mathbf{v} \cdot \mathbf{n}_\phi)^2 \end{aligned} \quad (63)$$

where the only penalization term is $\frac{1}{\eta} \rho (\mathbf{v} \cdot \mathbf{n}_\phi) \mathbf{n}_\phi$. A typical value for the penalization parameter is $\eta = 10^{-10}$, which accurately enforces the slip velocity ($\mathbf{v} \cdot \mathbf{n}_\phi = 0$) near the immersed boundary. As for the classic penalization method, $\mathbf{v} \cdot \mathbf{n}_\phi$ exponentially tend towards zero (almost instantaneously). This approach is suitable if the Euler equations are solved for a steady state.

It is also possible to use $\eta_c < 1$. In such a case, it is important to respect a ratio η/η_c as there is an interaction between the Neumann and Dirichlet conditions in the momentum equation. The idea is to keep the imposition of $\mathbf{v} \cdot \mathbf{n} = 0$ dominant over the propagation of the information. To do so, $\eta \ll \eta_c$, a ratio of $\eta/\eta_c = 10^{-6}$ was found to be sufficient for most applications.

With the CBVP-Hs method, two adjustable parameters are used: η and η_c . However, by defining $\eta_c = 1$ or $\eta_c \geq 10^6 \eta$ only one parameter is left (η). It is therefore easy to calibrate, just like the Volume Penalization method of §4.1. This is also an improvement over the CBVP method which has three adjustable parameters: η, η_c and ν_η .

4.4. Note on Accuracy

The volume penalization method is known to be 0^{th} order accurate in the imposition of the boundary condition, meaning only a global 1^{st} order accuracy can be achieved. Some extensions to second order accuracy are available in the literature [31, 32] by using information at the discrete level. Here the implementation is limited to the classical first order accuracy. With this type of approach, the accuracy of the method is usually improved by refining the mesh in the vicinity of the immersed boundary.

In the current implementation, even if the sharp Heaviside function leads to a staircase representation of the immersed boundary, the Neumann boundary conditions (convective terms) are smoothing the interface and improving the solution on coarser meshes. However, because of the staircase representation of the immersed boundary

and because the cell centers are used to determine if a cell is fluid or solid, the current implementation is not well suited to deal with sharp features (e.g. sharp trailing edge of an airfoil). In such a case, a refinement in the vicinity of the sharp feature must be done to capture it accurately. There are alternative ways to deal with this issue without increasing the cell count nor relying on adaptive meshing technique.

1. For the specific case of the sharp trailing edge, it is possible to simply approximate it as blunt. In this way, the cell refinement can be coarser while allowing the correct overall solution to be retrieved.
2. A second order volume penalization method [31, 32] could be implemented avoiding the staircase representation of the immersed boundary. However, because information is required at the discrete level the penalization method loses its discretization-independent character.
3. A smooth mask function (χ) like a smeared-out Heaviside function could be used. In this way, it would be possible for χ to have a value between 0 and 1, thus allowing cells intersected by the immersed boundary to be penalized even if the cell center is on the fluid side. However, this leads to a diffuse interface representation and an interaction between the Euler and immersed boundary fluxes which is difficult to control.
4. The selected approach for icing application is to deal with sharp features on the clean geometry using a body-fitted mesh (e.g. sharp trailing edge on an airfoil). Only the ice will be immersed in the mesh (see Figure 19b). Although some sharp features may be generated by the ice growth, it is acceptable for them to be slightly smoothed out.

4.5. Mesh Particularities

For unstructured meshes made of triangles, some cell configurations lead to a poor propagation of the information from the fluid to the solid. This situation occurs when a fluid cell near the immersed boundary is trapped between solid cells and the numerical fluxes allow no communication with neighboring fluid cells. One example is illustrated in Figure 3, where cell A is fluid and cell B is solid. Cell A has 2 solid cells and one fluid cell as direct face neighbors. In this specific configuration, cell A is emptied and the solution is propagated in the solid (e.g. cell B).

One solution is to apply a correction on the mask function (χ) for these pathological cells: instead of using a sharp definition ($\chi = 0$ or 1), χ is set to the solid fraction of the cell ($\chi \in [0, 1]$). This correction blends the Euler and the penalization fluxes leading to a smoother solution as the communication with the fluid is restored.

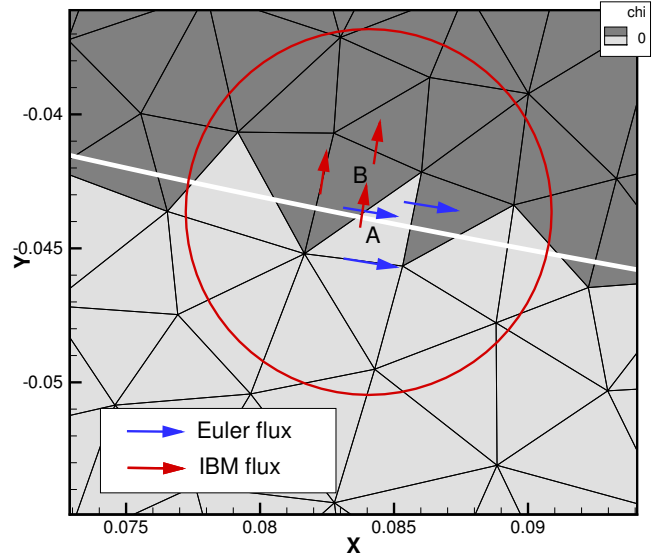


Figure 3: Pathological cell example with flux representation and mask function χ

From numerical experiments, the issue was observed for only a few cells (1% to 2% of the immersed boundary cells) and not for all meshes. Some unstructured meshes will present no pathological cells while for structured meshes made of quadrilateral cells, the issue was never observed. Also, note that the issue is present for both the CBVP and CBVP-Hs methods.

5. Results

In this section, the behavior of the CBVP-Hs method is shown on different test cases. A mesh refinement study is first performed for the weakly compressible flow around a circular cylinder. Then the subsonic flow around a NACA0012 airfoil is studied. The penalization method is also tested on an ice horn which was found difficult to solve in a previous communication [33] due to its high curvature. The simulation parameters are summarized in Table 1.

The solution from the penalization method is verified against analytical solutions when applicable or against numerical solutions obtained by a body-fitted approach. A comparison is also performed against the CBVP method. Wall pressure coefficients, entropy and total enthalpy errors are compared and discussed.

Table 1: Simulation Parameters

	Cylinder	Airfoil	Ice Horn
Geometry	Cylinder	NACA0012	GLC305
Chord	D=2.0	1.0	0.9144
AoA	0.0	1.25	4.0
Mach	0.1	0.5	0.273
P_{static}	100kPa	100kPa	101.325 kPa
T_{static}	300.0K	300.0K	268.3K
LWC	–	–	0.54g/m ³
MVD	–	–	20μm
Icing Time	–	–	1350s

In Table 1, LWC stands for Liquid Water Content and represents the mass of water per volume of air. The median volume diameter (MVD) represents the droplet size for the icing simulation. The list of icing parameters are provided but note that only the aerodynamics is treated in this paper.

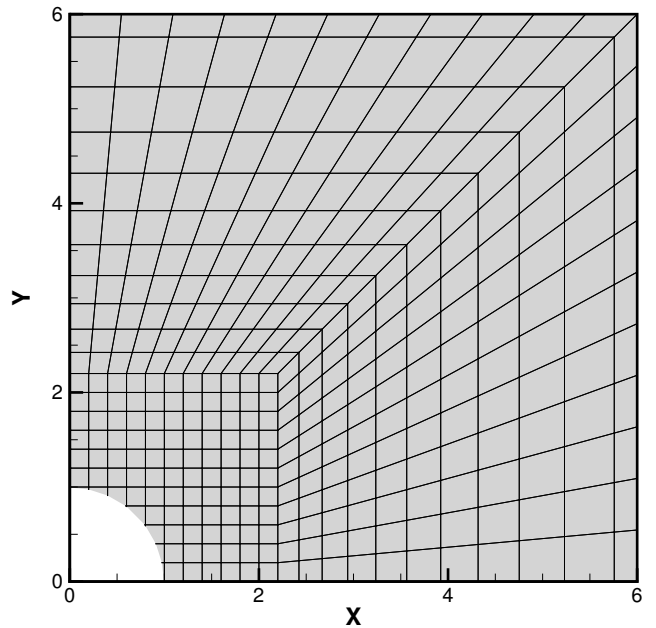
For the following simulations, the convergence is determined by monitoring the L_2 and L_∞ norms of the wall pressure coefficient (C_p). The usual density, momentum and energy residuals are also monitored. In the following sections, when the convergence threshold is specified, the criterion on C_p is used. For the penalization method, the convergence check requires a pressure interpolation at the immersed boundary at each time step. It is performed by a weighted least square interpolation method.

5.1. Weakly Compressible Flow Around a Cylinder

The first test case is the weakly compressible flow around a circular cylinder. As the Euler flow solver in IGLOO2D is compressible only, the incompressible analytical solution is approached by performing the simulation at a low Mach number (Mach= 0.1). The analytical solution for the pressure coefficient (C_p) is, in 2D Cartesian coordinates:

$$C_{p_{analytical}} = \frac{2R_c^2(x^2 - y^2) - R_c^4}{(x^2 + y^2)^2} \quad (64)$$

where R_c is the radius of the cylinder.

Figure 4: Mesh for the cylinder with cell size $D/\Delta x = 10$

A family of five meshes is generated ranging from $D/\Delta x = 10$ to $D/\Delta x = 160$, where D is the diameter of the cylinder and Δx the Cartesian cell size. The cylinder is immersed into a uniform Cartesian grid. To reduce the total number of cells the uniform Cartesian grid is limited to a width of 2 diameters. Outside this zone a structured mesh is used allowing cell growth and stretching, but still ensuring mesh symmetry. The far field is located at 50 diameters from the cylinder. Part of the mesh for $D/\Delta x = 10$ is illustrated in Figure 4 with a zoom on the blanked cylinder.

For the results presented below, the wall C_p residual is converged to 10^{-8} . Figures 5 and 6 illustrate the C_p distribution for both the CBVP and CBVP-Hs methods. From these figures, both methods converge towards the analytical solution. However, the mesh convergence is faster for the CBVP-Hs method for which a good global C_p distribution is achieved on a mesh as coarse as $D/\Delta x = 40$. In comparison, the CBVP method exhibits a satisfactory global solution for the finest mesh only ($D/\Delta x = 160$).

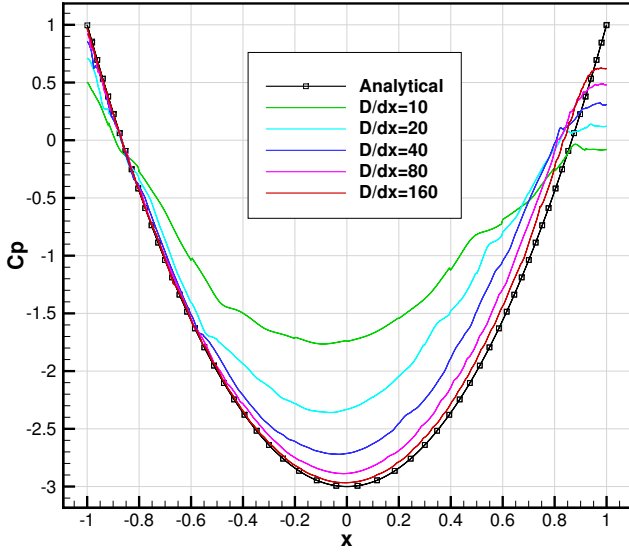


Figure 5: Wall C_p with mesh refinement for the cylinder (CBVP)

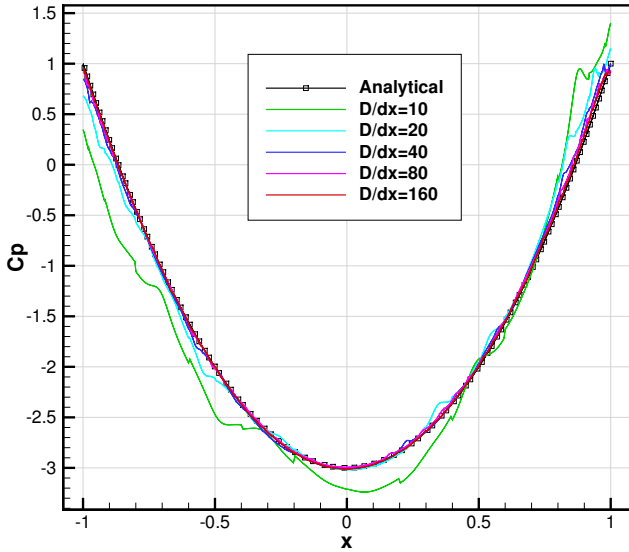


Figure 6: Wall C_p with mesh refinement for the cylinder (CBVP-Hs)

For a more detailed analysis, pressure coefficients are extracted and tabulated in Table 2 at locations of interest: $(x, y) = (-1, 0)$, $(x, y) = (0, 1)$ and $(x, y) = (1, 0)$. For these locations the expected analytical solution is respectively: $C_p = 1$, $C_p = -3$ and $C_p = 1$. For the finest mesh ($D/\Delta x = 160$), the CBVP captures the maximum suction ($C_p = -2.967$). The forward stagnation point at $x = -1$ is solved accurately with $C_p = 0.962$. However the aft stagnation point at $x = 1$ exhibits too much diffusion to reattach correctly and the analytical solution is not recovered ($C_p = 0.621$).

Using the CBVP-Hs a great improvement is achieved on the CBVP method. The suction peak is captured on

a mesh as coarse as $D/\Delta x = 20$ with $C_p \approx -3$. The reattachment point at $x = 1$ is captured much more accurately ($C_p = 0.914$, $D/\Delta x = 160$). The CBVP-Hs allows a less diffusive solution aft of the cylinder which explains the better reattachment behavior.

Table 2: C_p at specific wall locations for the cylinder

Location	$x = -1$	$x = 0$	$x = 1$
Analytical	$C_p = 1$	$C_p = -3$	$C_p = 1$
CBVP			
$D/\Delta x = 10$	5.048e-01	-1.738e+00	-8.052e-02
$D/\Delta x = 20$	7.095e-01	-2.335e+00	1.218e-01
$D/\Delta x = 40$	8.514e-01	-2.716e+00	3.095e-01
$D/\Delta x = 80$	9.241e-01	-2.888e+00	4.813e-01
$D/\Delta x = 160$	9.620e-01	-2.967e+00	6.213e-01
CBVP-Hs			
$D/\Delta x = 10$	3.465e-01	-3.207e+00	1.402e+00
$D/\Delta x = 20$	6.800e-01	-3.017e+00	1.154e+00
$D/\Delta x = 40$	8.450e-01	-3.008e+00	9.980e-01
$D/\Delta x = 80$	9.229e-01	-2.994e+00	9.301e-01
$D/\Delta x = 160$	9.618e-01	-3.009e+00	9.136e-01

The pressure coefficients from Table 2 are also illustrated on Figure 7 which shows the C_p error against the analytical solution for the three locations:

$$|\Delta C_p| = |C_p - C_{p_{analytical}}| \quad (65)$$

As the mesh is refined the error at $x = -1$ is roughly the same for both methods (CBVP and CBVP-Hs). However, the error is much lower at the maximum suction peak and at the aft stagnation point for the CBVP-Hs method. For the forward stagnation point, the order of convergence is observed to be 1 for both methods. It is, however, difficult to conclude on the order of convergence for the other locations. The order of convergence will be discussed based on global wall error estimates in the next section.

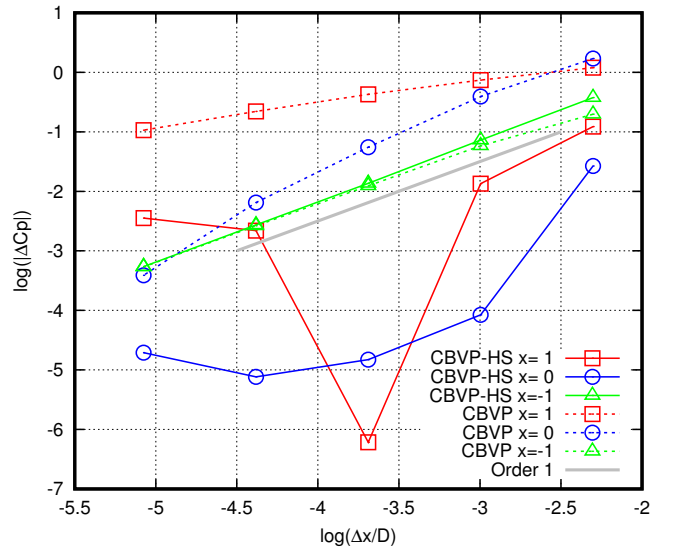


Figure 7: Cylinder ΔC_p convergence as the mesh is refined

5.1.1. Entropy and Total Enthalpy

As the flow around the cylinder presents no heat source nor external force, the entropy (s) and total enthalpy (H) should be conserved in the entire computational domain. Thus, entropy and total enthalpy errors can be evaluated against the freestream conditions as:

$$\Delta s = |(s - s_\infty)| / s_\infty \quad (66)$$

$$\Delta H = |(H - H_\infty)| / H_\infty \quad (67)$$

$$s_\infty = P_\infty / \rho_\infty^\gamma \quad (68)$$

$$H_\infty = \frac{\gamma}{\gamma - 1} \frac{P_\infty}{\rho_\infty} + \frac{1}{2} \|\mathbf{v}_\infty\|^2 \quad (69)$$

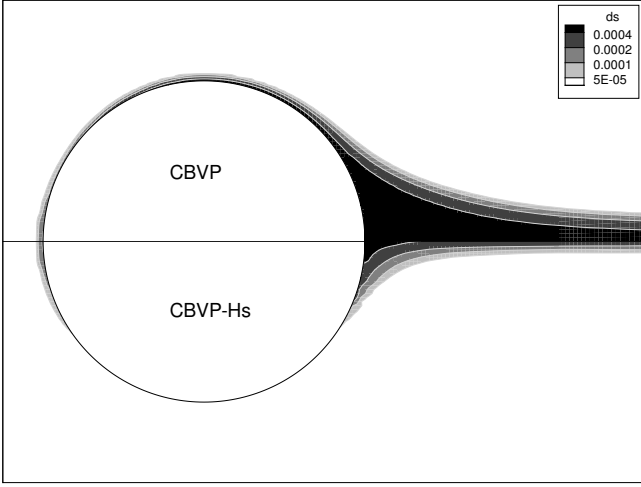


Figure 8: Entropy error for the cylinder on the Cartesian mesh $D/\Delta x = 80$. The cylinder is blanked for clarity.

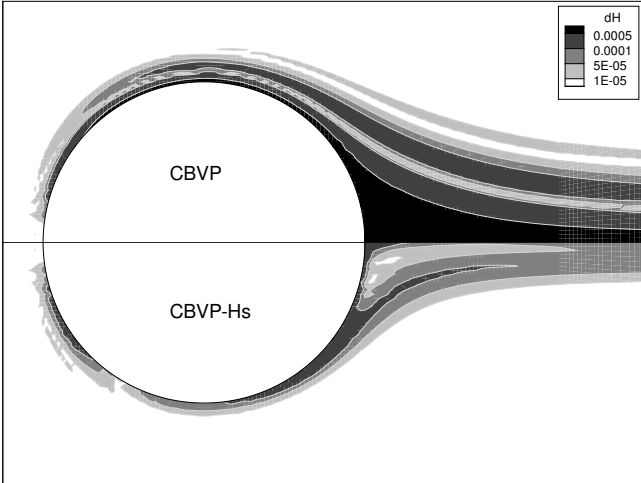


Figure 9: Total enthalpy error for the cylinder on the Cartesian mesh $D/\Delta x = 80$. The cylinder is blanked for clarity.

The contours for the entropy and total enthalpy error are illustrated on Figures 8–9. These figures confirm that the CBVP-Hs method reduces the error in the wake and at

the maximum suction points of the cylinder. However, the error is similar for both methods at the forward stagnation point. As an additional comparison point, the maximum entropy error in the field for the CBVP is $\approx 1e-3$ while it is $\approx 6e-4$ for the CBVP-Hs. The same behavior is observed for the total enthalpy error whose maximum is $\approx 1e-3$ for the CBVP and $\approx 3e-4$ for the CBVP-Hs. As a comparison, for a body-fitted simulation using an equivalent wall cell size the error for entropy and total enthalpy is respectively $\approx 1e-5$ and $\approx 8e-6$ using the CCST boundary condition.

Table 3: Error at the wall for the cylinder (L_2 norm)

Grid	RMS_H	RMS_s	RMS_Cp
CBVP			
$D/\Delta x = 10$	1.462e-03	1.356e-03	8.183e-01
$D/\Delta x = 20$	1.203e-03	1.074e-03	5.368e-01
$D/\Delta x = 40$	9.681e-04	7.472e-04	3.274e-01
$D/\Delta x = 80$	6.608e-04	4.702e-04	1.995e-01
$D/\Delta x = 160$	4.456e-04	3.071e-04	1.194e-01
CBVP-Hs			
$D/\Delta x = 10$	1.731e-03	1.853e-03	4.279e-01
$D/\Delta x = 20$	6.930e-04	6.738e-04	1.790e-01
$D/\Delta x = 40$	3.371e-04	3.395e-04	8.344e-02
$D/\Delta x = 80$	1.575e-04	1.482e-04	4.805e-02
$D/\Delta x = 160$	9.232e-05	6.329e-05	3.011e-02

The error at the wall for Cp , s and H are compiled in Table 3 for both methods and for the different refinement levels. The error is presented as the L_2 norm (RMS) ΔCp , Δs and ΔH respectively. This gives an indication of the global wall error and confirms that the CBVP-Hs is more accurate. In fact, the CBVP solution with $D/\Delta x = 160$ is equivalent to the CBVP-Hs with $D/\Delta x = 40$ in terms of global wall error.

For a more visual representation, the data from Table 3 is also illustrated in Figure 10. From this figure, the error is observed to be lower for the CBVP-Hs method while also offering a faster convergence rate on ΔH and Δs . The order of convergence is observed to be 1 for the CBVP-Hs method on entropy and total enthalpy, while it is slightly lower for the CBVP method. The volume penalization method is known to be 1st order accurate. Thus it is logical to obtain 1st order of convergence at best although the solution is 2nd order accurate in the field (2nd order Roe Scheme). Note that the Euler flow solver was verified to achieve 2nd order of convergence for a family of body fitted meshes (not shown in this paper).

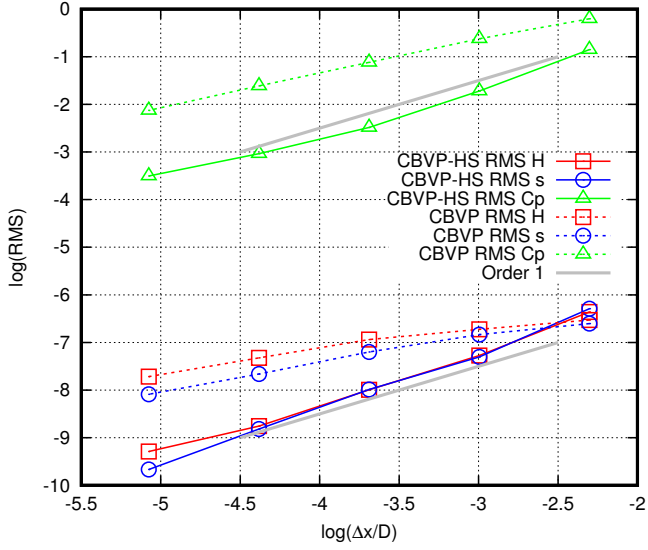


Figure 10: Global wall error (L_2 norm) for the cylinder

5.1.2. Continuity of the Solution

The cylinder case with $D/\Delta x = 80$ is used to illustrate the continuity of the solution in the vicinity of the immersed boundary and inside the solid zone. Both the CBVP and CBVP-Hs are designed with hyperbolic penalization terms on the continuity and energy equations allowing the propagation of information from the fluid to the solid in the normal direction to the interface. However, the two methods differ on the momentum equation where the continuity of the velocity is imposed by an artificial dissipation term for the CBVP and by a hyperbolic penalization term for the CBVP-Hs. For both methods, a no-penetration velocity ($\mathbf{v} \cdot \mathbf{n}_\phi = 0$) is enforced in the solid, thus only the tangential component of the velocity remains.

As shown on Figure 11, the tangential velocity is continuous across the immersed boundary for both methods. For the CBVP, the continuity is enforced via numerical dissipation. This does not only produce an unphysical extension of the tangential velocity in the solid, it also pollutes the solution in the fluid near the immersed boundary. On the other hand, the CBVP-Hs extends the tangential velocity following the physics of the wall streamline. Also note that the curvature terms are only activated in the vicinity of the interface, the remainder of the solid zone only sees convection terms in the direction normal to the immersed boundary. It translates into a proper extension of the fluid properties near the immersed boundary, then into straight contour lines pointing towards the center of the cylinder.

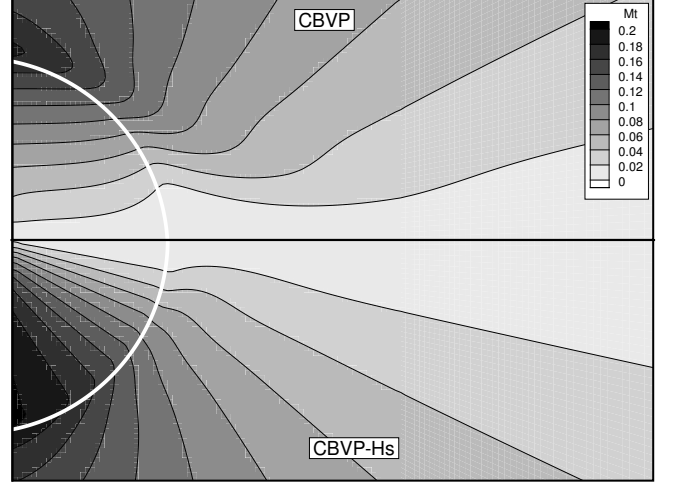


Figure 11: Continuity of the tangential Mach number (M_t) near the immersed boundary and inside the solid for both CBVP and CBVP-Hs ($D/\Delta x = 80$).

The continuity of the pressure (C_p) is illustrated on Figure 12. In terms of pressure both the CBVP and CBVP-Hs methods behave in a similar and satisfactory manner inside the solid. The main difference is coming from the quality of the solution, which is more accurate for the CBVP-Hs on an equivalent mesh.

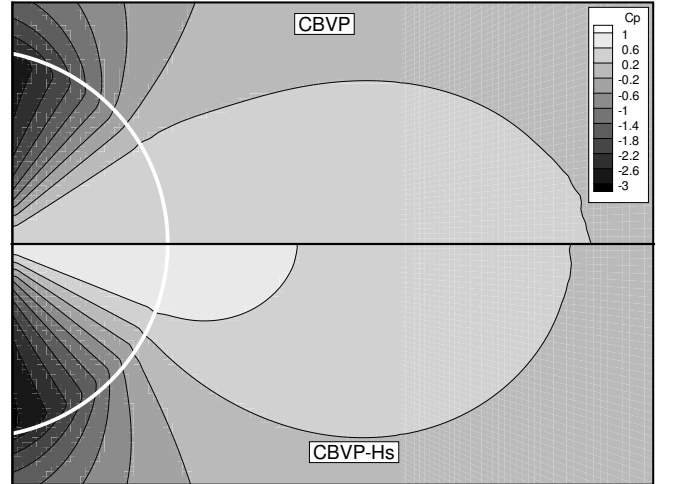


Figure 12: Continuity of the pressure coefficient (C_p) near the immersed boundary and inside the solid for both CBVP and CBVP-Hs ($D/\Delta x = 80$).

It is also interesting to verify the continuity of entropy and total enthalpy as it should be strongly imposed using the CBVP-Hs, the results are shown on Figures 13–14. Both methods propagate the entropy and total enthalpy from the fluid to the solid. The CBVP method exhibits larger error at the suction peak and aft of the cylinder on the fluid side. This error is also propagated into the solid. On the other hand, the CBVP-Hs method shows a non-dimensional solution closer to unity (more accurate) on the

fluid side. This is also reflected inside the solid as expected. These two figures emphasize the difference in accuracy of the two methods in the vicinity of the immersed boundary, with a better solution achieved by the CBVP-Hs.

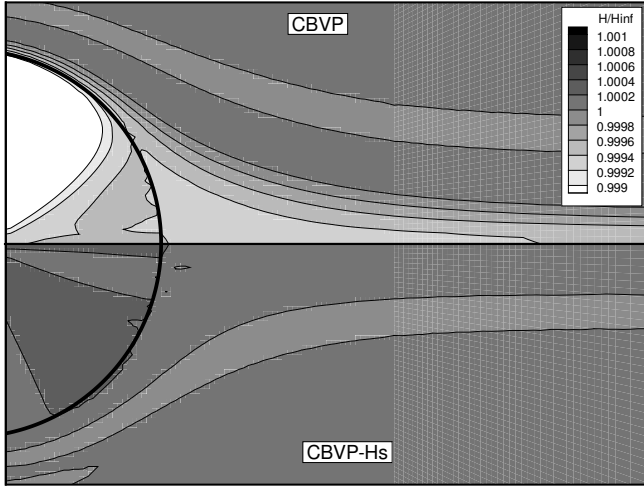


Figure 13: Continuity of the total enthalpy (H/H_{∞}) near the immersed boundary and inside the solid for both CBVP and CBVP-Hs ($D/\Delta x = 80$).

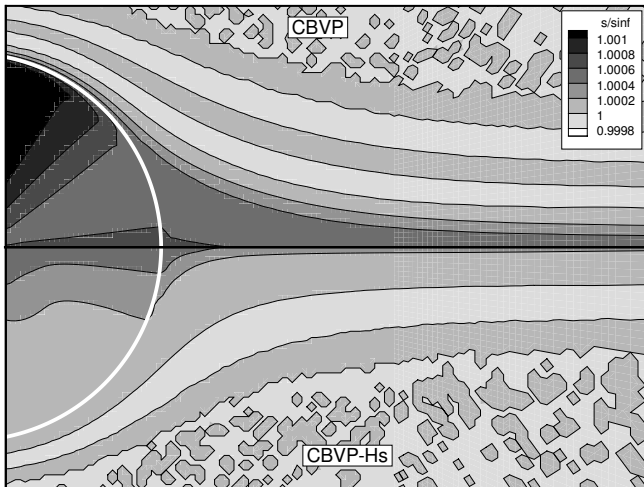


Figure 14: Continuity of the entropy (s/s_{∞}) near the immersed boundary and inside the solid for both CBVP and CBVP-Hs ($D/\Delta x = 80$).

5.2. Subsonic Flow Around a NACA0012

A more representative test case for aerospace applications is the subsonic flow around an airfoil. As stated earlier, the first order accurate penalization method is not well suited for the representation of sharp features like trailing edges. Here, the issue is worked around by using a NACA0012 airfoil with a blunt trailing edge, allowing easier meshing of the solid (interior mesh). An unstructured mesh is used to show that the method is also applicable to general meshes. Here, the penalization method

is compared to the solution obtained with a body-fitted approach.

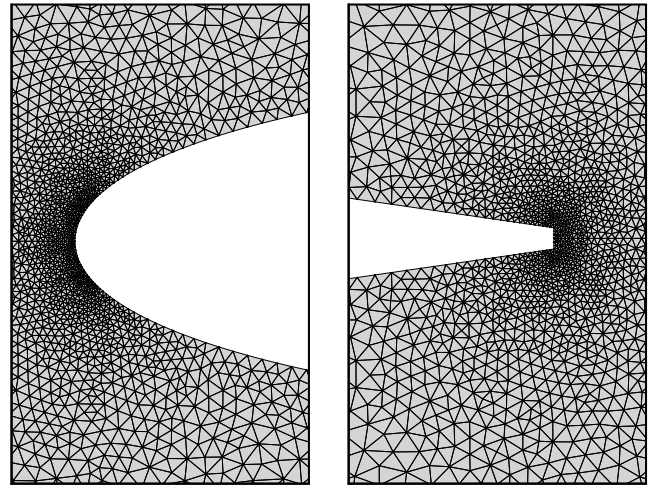


Figure 15: Body-fitted mesh for the NACA0012 airfoil with blunt trailing edge. Right: zoom on the leading edge. Left: zoom on the trailing edge.

The body-fitted and immersed boundary meshes are respectively shown in Figures 15–16. The meshes are refined at the leading and trailing edges and the far field is located at 50 chords from the airfoil. The same parameters are used to generate the immersed boundary and body-fitted meshes, ensuring comparable cell-sizes and refinement. In terms of the chord (c), the cell sizes at the wall, leading edge, trailing edge and far field are respectively: $5e-3c$, $1e-3c$, $1e-4c$ and $4c$. A linear cell size growth is allowed from the wall to the far field boundary. For the body-fitted and immersed boundary meshes, it gives a total of 42700 and 49850 cells respectively.

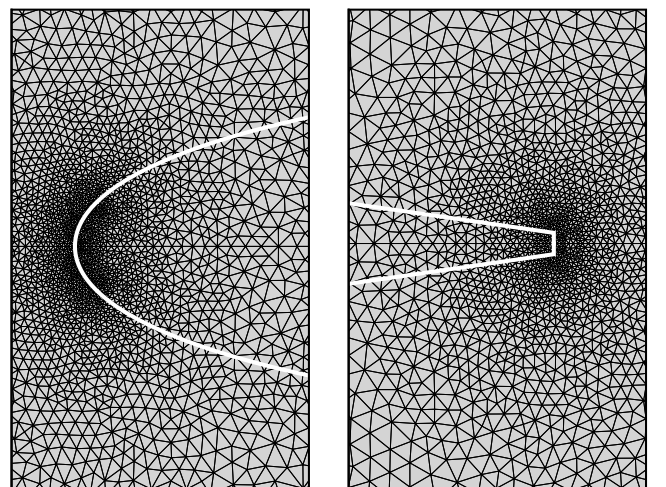
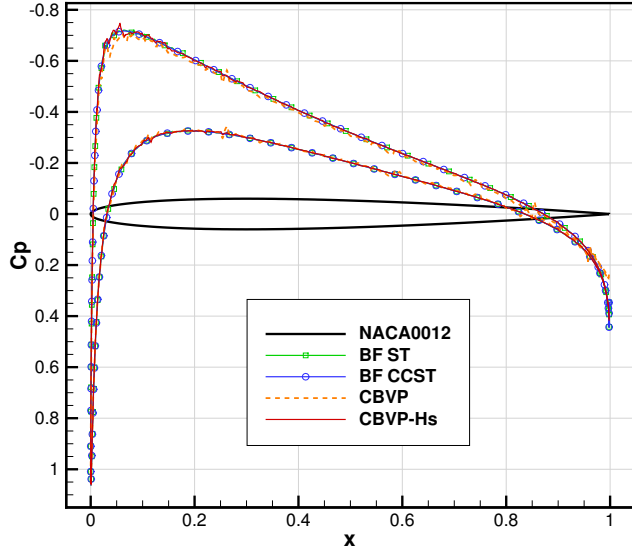
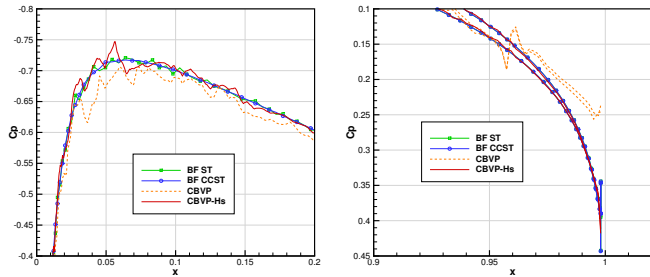


Figure 16: Immersed boundary mesh for the NACA0012 airfoil with blunt trailing edge. Right: zoom on the leading edge. Left: zoom on the trailing edge.

For this test case, the standard subsonic flow condition of $Mach = 0.5$ and $AoA = 1.25$ deg are used. To allow a fair comparison with the penalization methods, the body-fitted (BF) simulation is performed with both the ST and CCST wall boundary conditions. As a reminder, the CBVP and CBVP-Hs both account for the wall curvature, similar to the CCST.



(a) Global view



(b) Zoom near Cp_{max} (c) Zoom at the trailing edge

Figure 17: Wall C_p for the NACA0012 airfoil at $Mach=0.5$ and $AoA=1.25$ deg. Comparison to the BF ST and BF CCST.

The results from Figure 17 illustrate the C_p distribution at the wall. For the body-fitted results, the ST and CCST provide almost the same solution except the CCST boundary condition provides smoother results (Figure 17b). On a geometry with moderate curvature and using a mesh with adequate refinement both the ST and CCST are expected to be equivalent. This is in line with the observations of Figure 17. The lift coefficients for the body-fitted solutions are respectively $C_L = 0.1766$ and $C_L = 0.1768$ for the ST and CCST boundary conditions.

Now considering the penalization methods, the C_p distribution for the CBVP method is close to the body-fitted solution with a slight overestimation in the vicinity of the maximum suction. Also, the pressure coefficient is not as accurate at the trailing edge for this method. On the other

hand, the C_p distribution for the CBVP-Hs fits well with the body-fitted results. Its behavior is closer to the ST boundary condition, exhibiting small oscillations. The lift coefficients are respectively $C_L = 0.1630$ and $C_L = 0.1760$ for the CBVP and CBVP-Hs. Again the CBVP-Hs is much closer to the body-fitted solution ($C_L \in [0.1766, 0.1768]$). This result shows that this penalization method is able to perform well on an airfoil case if the mesh is sufficiently refined and if sharp features are treated adequately. It also confirms that the method is suitable for unstructured grids.

5.3. Flow Around an Ice Horn

Ice shape can be very challenging for mesh generation and for the flow solver. One particular case that was found difficult to deal with in a previous communication [33] is the ice horn generated by the conditions listed in Table 1. This ice shape exhibits an ice horn of high curvature which can lead to flow separation, even with a Euler flow solver. This behavior is shown in Figure 18, where the simulation is performed using the body-fitted mesh of Figure 19a and the ST wall boundary condition.

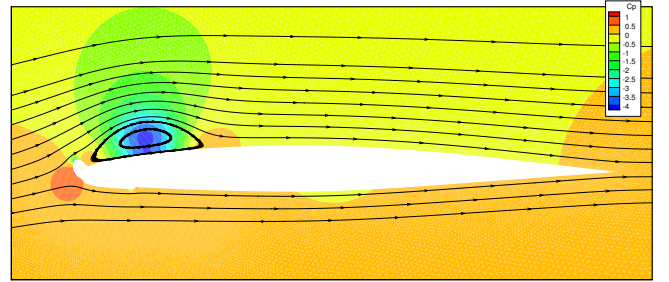
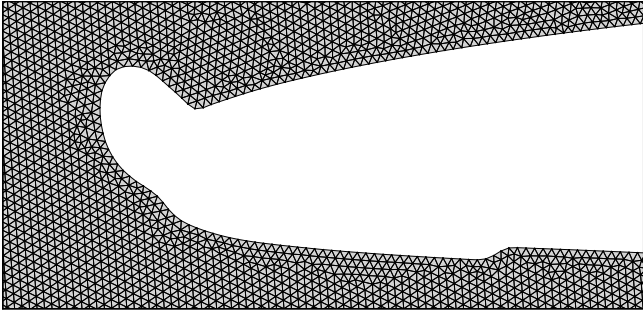


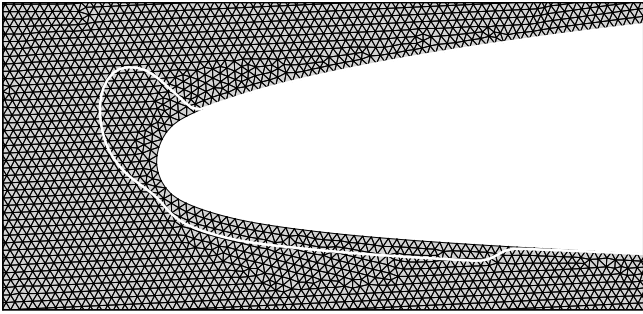
Figure 18: Field of C_p contours and velocity streamtraces for the ice horn case using a body-fitted mesh and the ST wall boundary condition

For this test case, the strategy is to use a body fitted mesh for the clean geometry (GLC305) and to use an immersed boundary to account for the ice shape (Figure 19b). In this way, the sharp trailing edge is solved accurately and the ice shape can be dealt with to first order accuracy (penalization).

Here, the Euler flow is solved on the ice accreted GLC305 for a 675s icing time (1st step of a 2-step multi-step process). The body-fitted and immersed boundary meshes around the ice horn are shown in Figure 19. Again the same cell size is used in the vicinity of the wall for both cases to allow a fair comparison. For this test case, the wall C_p is converged to 10^{-6} .



(a) Body-Fitted



(b) Immersed Boundary

Figure 19: Mesh around the ice horn

The C_p distribution on the ice horn is compared in Figure 21. First, the body-fitted solutions using the two types of wall boundary conditions are examined: ST and CCST. The ST was previously shown to give a separated flow Figure 18 which can now be observed on Figure 21. This flow separation is induced by the numerical viscosity of the flow solver and has no physical meaning. It would be preferable to obtain an attached solution to be in line with the theory of inviscid flows. Numerical experiments showed that a significantly finer mesh would be required to obtain an attached solution with the ST.

An alternative approach is to apply the CCST to account for the wall curvature and therefore increase the accuracy of the solution on coarser mesh. On Figures 20–21, it is shown that the use of the CCST indeed leads to an attached flow solution on the current mesh. This also significantly increases the suction peak at the ice horn tip which is now at $C_p \approx -13$ in comparison to $C_p \approx -3$ for the ST approach.

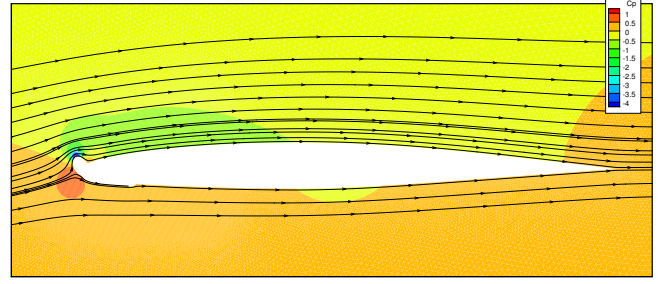
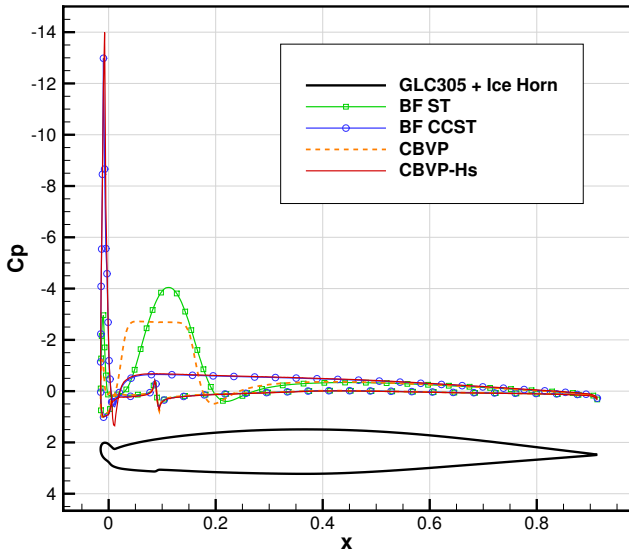
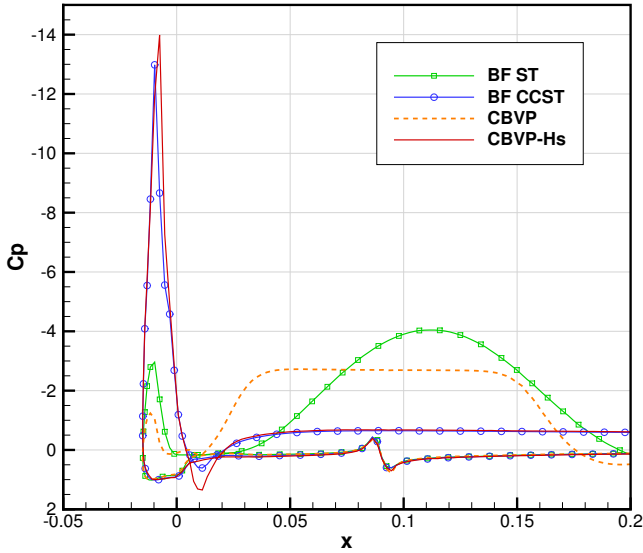


Figure 20: Field C_p contours and velocity streamtraces for the ice horn case using a body-fitted mesh and the CCST wall boundary condition



(a) Global view



(b) Zoom near the ice horn

Figure 21: Wall C_p for the ice horn, comparison to the BF ST and BF CCST.

The results from the penalization methods are examined next: CBVP and CBVP-Hs. Both methods account for the wall curvature in the imposition of the wall boundary condition. However, as shown on Figure 21, the CBVP still exhibits flow separation on the ice horn case while the CBVP-Hs does not. This behavior is similar to the results obtained earlier on the cylinder, where the CBVP-Hs was more accurate and behaved better aft of the cylinder for coarser meshes. Again, it suggests that the CBVP would give similar results if the mesh was refined.

The difference between the two methods could be explained by the higher diffusivity of the CBVP and the fact that it does not specifically conserve entropy and total en-

thalpy. Also the CBVP-Hs better impose the streamline conditions near the immersed boundary. The CBVP-Hs follows the boundary conditions imposed by the CCST and exhibits similar behavior on the ice horn case. From the previous observations, the CBVP-Hs is concluded to be more accurate and more suitable for geometries with high curvature and therefore, for ice accretion simulations.

5.4. Transonic Flow Around a NACA0012

Another interesting test case for aerospace applications is the transonic flow over an airfoil. The flow around a NACA0012 airfoil at $Mach = 0.8$ and $AoA = 1.25$ deg is computed. The comparison is performed between the standard Body-Fitted mesh approach and the CBVP-Hs.

It is first observed that the solutions obtained with the body-fitted ST and CCST boundary conditions are very close with a lift coefficient of $C_L = 0.3464$ and $C_L = 0.3462$, respectively.

The results of Figure 22 show that for a mesh of comparable refinement, the CBVP-Hs is able to capture the shock location with reasonable accuracy. The lift coefficient for the CBVP-Hs is $C_L = 0.3423$ which is not far from the body-fitted results. A better C_L could be obtained by properly refining the mesh in the vicinity of the shocks. However, it still shows the potential of the CBVP-Hs for the simulation of transonic and supersonic flows.

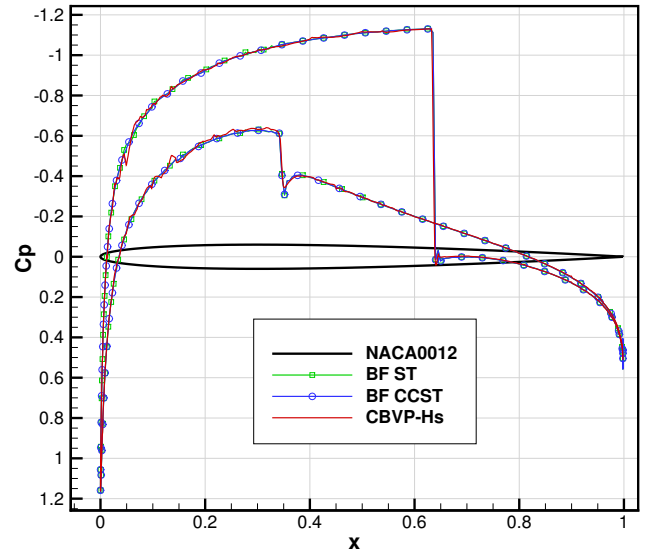


Figure 22: Wall C_p for the NACA0012 airfoil at $Mach = 0.8$ and $AoA = 1.25$ deg. Comparison to the BF ST and BF CCST.

6. Conclusion

In this paper, a penalization method which conserves entropy and total enthalpy is developed for the Euler equations with icing applications.

Two types of numerical wall boundary conditions are described for body-fitted meshes: the symmetry technique

(ST) and curvature-corrected symmetry technique (CCST). For the immersed boundary method, the penalization is selected for its simplicity of implementation and its mesh and discretization independence. The penalization method is usually applied to the Navier-Stokes equations and applications to the Euler equations are few. The characteristic-based volume penalization (CBVP) of [23] showed to be suitable for most cases but exhibits too much diffusivity in some icing application with high curvature geometries. A new method is thus developed, the CBVP-Hs, which can be seen as the application of the CCST boundary conditions using the penalization method.

The body-fitted and penalization methods are tested on several test cases. A mesh convergence is performed for the weakly compressible flow around a circular cylinder. Then the subsonic and transonic flows around a NACA0012 airfoil are solved. Also, the airflow around an ice horn of high curvature is evaluated to assess the methods on a challenging icing case.

The CBVP and CBVP-Hs are found to perform well for the Euler equations. However, the CBVP method exhibits a more diffusive solution with higher error level on the pressure coefficient, conservation of total enthalpy and conservation of entropy compared to the CBVP-Hs. The CBVP-Hs is also found to be more accurate on coarser meshes. For instance on the cylinder, the CBVP-Hs solution on the $D/\Delta x = 40$ mesh is equivalent to the CBVP on the $D/\Delta x = 160$ mesh. For the ice horn case and for the same mesh refinement, the CBVP exhibits flow separation while the flow remains attached for the CBVP-Hs, which is more in line with inviscid flow theory. Also, the CBVP-Hs shows a good potential for the simulation of transonic flows as it can capture the same shock location as a Body-Fitted simulation of comparable mesh refinement.

It is concluded that the application of the penalization method to the Euler equations requires special care to obtain accurate solutions on complex geometries. The newly developed approach (CBVP-Hs) proved to be a suitable candidate for this purpose.

Acknowledgments

This work is supported by the Natural Sciences and Engineering Research Council of Canada (NSERC) and the ONERA, the French Aerospace Lab.

References

- [1] J. M. Diebold, A. P. Broeren, M. Bragg, Aerodynamic classification of swept-wing ice accretion, in: Fluid Dynamics and Co-located Conferences, American Institute of Aeronautics and Astronautics, 2013, pp. –, also NASA/TM–2013-216556. doi:10.2514/6.2013-2825. URL <https://doi.org/10.2514/6.2013-2825>
- [2] P. Trontin, G. Blanchard, A. Kontogiannis, P. Villedieu, Description and assessment of the new onera 2D icing suite IGLOO2D, in: 9th AIAA Atmospheric and Space Environments Conference, 2017. doi:10.2514/6.2017-3417.
- [3] D. K. Clarke, H. A. Hassan, M. D. Salas, Euler calculations for multielement airfoils using cartesian grids, AIAA Journal 24 (3) (1986) 353–358. doi:10.2514/3.9273.
- [4] M. Berger, R. Leveque, An adaptive cartesian mesh algorithm for the euler equations in arbitrary geometries, in: Fluid Dynamics and Co-located Conferences, American Institute of Aeronautics and Astronautics, 1989, pp. –. doi:10.2514/6.1989-1930.
- [5] M. Berger, M. Aftosmis, Progress towards a cartesian cut-cell method for viscous compressible flow, in: 50th AIAA Aerospace Sciences Meeting, 2012, aIAA 2012-1301. doi:doi.org/10.2514/6.2012-1301.
- [6] J. Mohd-Yusof, Combined immersed-boundary/B-spline methods for simulations of flow in complex geometries, Annual Research Briefs, Center for Turbulence Research (1997) 317–328. URL <https://ntrs.nasa.gov/archive/nasa/casi.ntrs.nasa.gov/19990063249.pdf>
- [7] R. Mittal, H. Dong, M. Bozkurtas, F. Najjar, A. Vargas, A. von Loebbecke, A versatile sharp interface immersed boundary method for incompressible flows with complex boundaries, Journal of Computational Physics 227 (10) (2008) 4825 – 4852. doi:http://dx.doi.org/10.1016/j.jcp.2008.01.028.
- [8] R. P. Fedkiw, T. Aslam, B. Merriman, S. Osher, A non-oscillatory eulerian approach to interfaces in multimaterial flows (the ghost fluid method), Journal of Computational Physics 152 (2) (1999) 457 – 492. doi:http://dx.doi.org/10.1006/jcph.1999.6236.
- [9] C. S. Peskin, Flow patterns around heart valves: A numerical method, Journal of Computational Physics 10 (2) (1972) 252–271. doi:http://dx.doi.org/10.1016/0021-9991(72)90065-4.
- [10] P. Angot, C.-H. Bruneau, P. Fabrie, A penalization method to take into account obstacles in incompressible viscous flows, Numerische Mathematik 81 (4) (1999) 497–520. doi:10.1007/s002110050401.
- [11] R. Mittal, G. Iaccarino, Immersed boundary methods, Annual Review of Fluid Mechanics 37 (2005) 239–261. doi:10.1146/annurev.fluid.37.061903.175743.
- [12] F. Sotiropoulos, X. Yang, Immersed boundary methods for simulating fluid–structure interaction, Progress in Aerospace Sciences 65 (2014) 1 – 21. doi:http://dx.doi.org/10.1016/j.paerosci.2013.09.003.
- [13] E. Arquis, J. P. Caltagirone, Sur les conditions hydrodynamiques au voisinage d’une interface milieu fluide - milieu poreux: application à la convection naturelle, in: C. R. Acad. Sci. Paris, Vol. 299 of série II, 1984, pp. 1–4.
- [14] J. P. Caltagirone, E. Arquis, Recirculations en milieu poreux, in: C. R. Acad. Sci. Paris, Vol. 302 of série II, 1986.
- [15] H. Beaugendre, F. Morency, F. Gallizio, S. Laurens, Computation of ice shedding trajectories using cartesian grids, penalization, and level sets, Model. Simul. Eng. 2011 (2011) 3:1–3:15. doi:10.1155/2011/274947.
- [16] H. Beaugendre, F. Morency, Innovative model for flow governed solid motion based on penalization and aerodynamic forces and moments, Research Report RR-8718, INRIA Bordeaux, équipe CARDAMOM ; IMB ; INRIA (Apr. 2015). URL <https://hal.inria.fr/hal-01144855>
- [17] Q. Liu, O. V. Vasilyev, A Brinkman penalization method for compressible flows in complex geometries, Journal of Computational Physics 227 (2) (2007) 946 – 966. doi:http://dx.doi.org/10.1016/j.jcp.2007.07.037.
- [18] E. Feireisl, J. Neustupa, J. Stebel, Convergence of a Brinkman-type penalization for compressible fluid flows, Journal of Differential Equations 250 (1) (2011) 596 – 606. doi:http://dx.doi.org/10.1016/j.jde.2010.09.031.
- [19] R. Abgrall, H. Beaugendre, C. Dobrzynski, An immersed boundary method using unstructured anisotropic mesh adaptation combined with level-sets and penalization techniques, Journal of Computational Physics 257 (2014) 83 – 101. doi:http://dx.doi.org/10.1016/j.jcp.2013.08.052.
- [20] L. Nouveau, Adaptive residual based schemes for solving the penalized Navier Stokes equations with moving bodies: appli-

- cation to ice shedding trajectories, Theses, Université de Bordeaux (Dec. 2016).
 URL <https://tel.archives-ouvertes.fr/tel-01500093>
- [21] A. Piquet, O. Roussel, A. Hadjadj, A comparative study of Brinkman penalization and direct-forcing immersed boundary methods for compressible viscous flows, *Computers & Fluids* 136 (2016) 272–284. doi:<https://doi.org/10.1016/j.compfluid.2016.06.001>.
- [22] O. Boiron, G. Chiavassa, R. Donat, A High-Resolution Penalization Method for large Mach number Flows in the presence of Obstacles, *Computers and Fluids* 38 (3) (2009) 703–714. doi:[10.1016/j.compfluid.2008.07.003](https://doi.org/10.1016/j.compfluid.2008.07.003).
- [23] E. Brown-Dymkoski, N. Kasimov, O. V. Vasilyev, A characteristic based volume penalization method for general evolution problems applied to compressible viscous flows, *Journal of Computational Physics* 262 (2014) 344–357. doi:<https://doi.org/10.1016/j.jcp.2013.12.060>.
- [24] E. Brown-Dymkoski, N. Kasimov, O. V. Vasilyev, A characteristic-based volume penalization method for arbitrary mach flows around solid obstacles, in: J. Fröhlich, H. Kuerten, B. J. Geurts, V. Armenio (Eds.), *Direct and Large-Eddy Simulation IX*, Springer International Publishing, Cham, 2015, pp. 109–115.
- [25] A. Dadone, B. Grossman, Surface boundary conditions for the numerical solution of the euler equations, *AIAA Journal* 32 (2) (1994) 285–293. doi:[10.2514/3.11983](https://doi.org/10.2514/3.11983).
- [26] A. Dadone, B. Grossman, Ghost-cell method for inviscid two-dimensional flows on cartesian grids, *AIAA Journal* 42 (12) (2004) 2499–2507. doi:<http://dx.doi.org/10.2514/1.697>.
- [27] A. Dadone, B. Grossman, Ghost-cell method for analysis of inviscid three-dimensional flows on cartesian-grids, *Computers & Fluids* 36 (10) (2007) 1513–1528, special Issue Dedicated to Professor Michele Napolitano on the Occasion of his 60th Birthday. doi:<https://doi.org/10.1016/j.compfluid.2007.03.013>.
- [28] Z. J. Wang, Y. Sun, Curvature-based wall boundary condition for the euler equations on unstructured grids, *AIAA Journal* 41 (1) (2003) 27–33. doi:[10.2514/2.1931](https://doi.org/10.2514/2.1931).
- [29] P. J. Schneider, D. H. Eberly, Chapter 13 - computational geometry topics, in: D. H. SCHNEIDER, PHILIP J. and EBERLY (Ed.), *Geometric Tools for Computer Graphics*, The Morgan Kaufmann Series in Computer Graphics, Morgan Kaufmann, San Francisco, 2003, pp. 673–825. doi:<https://doi.org/10.1016/B978-155860594-7/50016-3>.
- [30] Y. Bae, Y. J. Moon, On the use of Brinkman penalization method for computation of acoustic scattering from complex boundaries, *Computers & Fluids* 55 (2012) 48–56. doi:<https://doi.org/10.1016/j.compfluid.2011.10.015>.
 URL <http://www.sciencedirect.com/science/article/pii/S0045793011003215>
- [31] A. Etcheverlepo, Développement de méthodes de domaines fictifs au second ordre, Ph.D. thesis, Université Bordeaux I (2013).
 URL http://ori-oai.u-bordeaux1.fr/pdf/2013/ETCHEVERLEPO_ADRIEN_2013.pdf
- [32] A. Sarthou, S. Vincent, J. Caltagirone, A second-order curvilinear to cartesian transformation of immersed interfaces and boundaries. application to fictitious domains and multiphase flows, *Computers & Fluids* 46 (1) (2011) 422–428, 10th ICFD Conference Series on Numerical Methods for Fluid Dynamics (ICFD 2010). doi:<http://dx.doi.org/10.1016/j.compfluid.2010.11.008>.
- [33] P. Lavoie, G. Blanchard, E. Radenac, E. Laurendeau, P. Villedieu, A penalization method for 2d ice accretion simulations, in: *SAE Technical Paper*, SAE International, 2019. doi:[10.4271/2019-01-1939](https://doi.org/10.4271/2019-01-1939).